SHIP AND PROPULSOR HYDRODYNAMICS

Mattias Liefvendahl[*], Niklas Alin[*], Michel Chapuis[*], Christer Fureby[*], Urban Svennberg[*] and Carl Troëng[*]

[*]Swedish Defence Research Agency, FOI
147 25 Tumba, Sweden
e-mail: mattias.liefvendahl@foi.se

Key words: Large Eddy Simulation, Moving Grids, Finite Volume Method, Naval Hydrodynamics, Marine Propulsion

Abstract. *We present a computational approach for ship hydrodynamics and demonstrate its capabilities for selected problems in this field. A characteristic feature is to address unsteady aspects of the flow with Large Eddy Simulation, which have been validated against measurements for a wide range of cases. We employ a novel method, which relies on deformation and regeneration of the grid, to account for moving parts, rudders or propeller. The developments presented are based on the open source software package OpenFOAM, which provides an object-oriented library, based on the finite volume method, which is specially designed to facilitate the implementation of CFD-solvers.*

The following computational studies are presented, the majority of which contains validation with experimental data. (i) A model problem for the separation of a turbulent boundary layer at a smooth surface. (ii) Investigation of the near wake flow of a submarine propeller in stand-alone condition. (iii) Simulation of a submarine hull-propeller configuration, with a complete geometrical model for the propeller. (iv) Flow around a surface combatant, including simulation of the water surface and wave pattern.

1   INTRODUCTION

The field of naval hydrodynamics contains a wide range of computationally challenging problems, featuring very high Reynolds number flow, two-phase flow (water surface and cavitation) and the necessity to model moving components (maneuvering vessel, propeller and/or rudder motion). The aim of the present paper is to review the activities and tools, for ship and propulsor hydrodynamics, which have been developed at FOI. For the propulsion system, the two main design criteria are to improve the propulsive efficiency and to reduce the generated noise. For both, it is required to consider not only the propeller and hull separately but also to take into account their mutual interaction. In military applications the noise aspect is relatively more important. For these applications, we focus on the use of Large Eddy Simulation (LES), and the inhouse use of the OpenFOAM software library to implement modeling and develop new solvers.

As computers and computational methods continue to develop, the possibilities of using Computational Fluid Dynamics (CFD) in the ship design process is rapidly increasing. Potential flow methods, and even simpler methods, are used regularly, whereas viscous calculations, using Reynolds Averaged Navier-Stokes (RANS) models[5], are rapidly becoming feasible with respect both to the necessary computational resources and the achieved accuracy. Scale-model tests usually provide resistance and powering curves, which are difficult for computations to reproduce, as well as providing detailed data in important regions. Computations provide an overall picture of the flow that can help in its understanding and thus also in the hull/propulsor development process. A combination of model tests and computations appears to be the best approach to develop novel hull and propulsor concepts, and should be promoted even further. However, even RANS have limitations, mainly for applications where small-scale and/or unsteady flow phenomena are of interest but also when new, innovative designs are developed, the reliability of RANS may be problematic. This has been reported not only for academic test cases[10], but also for engineering applications[16]. Using LES-techniques instead of RANS, diminishes these problems and is today extensively used in aerospace and combustion, but due to the high Reynolds numbers in ship hydrodynamics, the interest for LES in this community is narrower. However, LES is rapidly becoming feasible for marine flows, at least as a tool to revisit designs and study flow features previously not available from RANS or experiments and learn from these.

The paper is organized as follows. First, we give an overview of the most important components of our computational methodology for ship hydrodynamics. In separate sections we treat LES subgrid modeling, the finite volume method and a moving mesh method. Then we demonstrate the simulation capability at FOI in this area, with the following four computational investigations, which are presented in separate sections of the paper. *(i)* A validation case for the investigation of unsteady separation at a three dimensional, curved smooth surface, It is well known that this phenomenon is difficult to predict computationally, and at the same time it occurs in a large number of applications. *(ii)*

A submarine propeller investigated in open water conditions. *(iii)* A completely coupled propeller-hull submarine model. To account for the moving component, we use a method which deforms and regenerates the computational grid during the propeller rotation[21]. *(iv)* A surface combatant, which require the simulation of the water surface, using the volume-of-fluid formulation, and which employs actator discs to model the effect of the two propellers. Data from measurements are available for validation of the computational results, for most of the configurations and computed quantities.

2 OVERVIEW OF COMPUTATIONAL METHODOLOGY FOR NAVAL HYDRODYNAMICS

We give an overview of the LES techniques we apply, the underlying finite volume method for the discretization of the flow equations and the moving grid method which allows for the simulation of moving components, in particular a rotating propeller attached to the hull. Due to lack of space, we do not include a description of the volume-of-fluid implementation[27], which allows for the inclusion of the water surface in the simulation, or the implementation of so-called actuator discs which describe the effect of a propulsor without a geometrical model of it.

2.1 LES subgrid modeling

In this section, we illustrate the derivation of the established explicit subgrid models we employ. In the application sections, we also include results obtained with RANS, DES (Detached Eddy Simulation) and the LES subgrid models DSMG (Dynamic Smagorinsky) and a LDKM, a localized dynamic model. We contrast explicit subgrid models with Implicit LES[20], which associates the subgrid model with the discretization of the convective term in the flow equations.

The conventional way of deriving the LES equations is to apply a low pass filtering operation to the incompressible Navier-Stokes equations[18], resulting in

$$\begin{cases} \partial_t \overline{\mathbf{v}} + \nabla \cdot (\overline{\mathbf{v}} \otimes \overline{\mathbf{v}}) = -\nabla \overline{p} + \nabla \cdot (\overline{\mathbf{S}} - \mathbf{B}) + \mathbf{m}, \\ \nabla \cdot \overline{\mathbf{v}} = m, \end{cases} \tag{1}$$

where $\overline{\mathbf{v}}$ is velocity, $\overline{p}$ the pressure, $\overline{\mathbf{S}} = 2\nu\overline{\mathbf{D}}$ the viscous strain tensor, $\overline{\mathbf{D}} = \frac{1}{2}(\nabla \overline{\mathbf{v}} + \nabla \overline{\mathbf{v}}^T)$ the rate of strain tensor, and ν the kinematic viscosity. Here, variables with overbar denote filtered quantities. The new terms appearing in the LES equations are due to the filtering of the non-linear terms in the Navier-Stokes equations and consists of the subgrid stress tensor $\mathbf{B} = \overline{\mathbf{v} \otimes \mathbf{v}} - \overline{\mathbf{v}} \otimes \overline{\mathbf{v}}$ and the commutation error terms m and $\mathbf{m}$. These latter two terms reflect the fact that filtering and differentiation do not generally commute but their effect can be considered small compared with the subgrid stress tensor and will be neglected. This leaves $\mathbf{B}$ to be modeled.

For the explicit modeling we first describe the One Equation Eddy Viscosity Model, OEEVM[1]. A transport equation for the subgrid kinetic energy k is solved together with

3

the LES equations,

$$\partial_t k + \nabla \cdot (k\overline{\mathbf{v}}) = 2\nu_{SGS}||\overline{\mathbf{S}}||^2 + \nabla \cdot (\nu_{eff}\nabla k) - \epsilon \tag{2}$$

and the eddy viscosity is computed as,

$$\nu_{SGS} = c_k \Delta k^{1/2}, \tag{3}$$

where $\epsilon = c_\epsilon k^{3/2}/\Delta$ is the dissipation and c_ϵ and c_k are model parameters based on an assumed inertial subrange behavior. Δ is a characteristic cell spacing (the LES filter width).

Alternatively, Bensow and Fureby[19] have proposed the following formulation,

$$\begin{cases} \partial_t \overline{\mathbf{v}} + \nabla \cdot (\overline{\mathbf{v}} \otimes \overline{\mathbf{v}} + \overline{\overline{\mathbf{v}} \otimes \overline{\mathbf{v}}} - \overline{\mathbf{v}} \otimes \overline{\mathbf{v}}) = -\nabla \overline{p} + \nabla \cdot (\overline{\mathbf{S}} - \tilde{\mathbf{B}}), \\ \nabla \cdot \overline{\mathbf{v}} = 0. \end{cases} \tag{4}$$

Here, the computable term $\tilde{\mathbf{L}} = \overline{\overline{\mathbf{v}} \otimes \overline{\mathbf{v}}} - \overline{\mathbf{v}} \otimes \overline{\mathbf{v}}$, a modified form of the Leonard tensor, has been extracted from the subgrid stress tensor $\mathbf{B}$ and is explicitly stated in the LES equations. This decomposition can easily be derived by inserting the velocity decomposition $\mathbf{v} = \overline{\mathbf{v}} + \mathbf{v}'$ into $\mathbf{B}$ yielding the composition $\mathbf{B} = \tilde{\mathbf{L}} + \tilde{\mathbf{B}} = \tilde{\mathbf{L}} + \tilde{\mathbf{C}} + \tilde{\mathbf{R}}$, where $\tilde{\mathbf{L}}$ represents the interaction of the smallest resolved scales, $\tilde{\mathbf{C}}$, the interaction between the smallest resolved and the largest unresolved scales, and $\tilde{\mathbf{R}}$ the mainly dissipative action of the smallest scales. This decomposition is similar to the ordinary Leonard descompostion, but all terms are now individually frame invariant thus allowing both the extraction of the $\tilde{\mathbf{L}}$ term and the individual modeling of $\tilde{\mathbf{C}}$ and $\tilde{\mathbf{R}}$. It can be argued[19] that traditional eddy viscosity models actually models only the dissipative action of $\tilde{\mathbf{R}}$ and neglects $\tilde{\mathbf{L}}$ and $\tilde{\mathbf{C}}$. We remark that the computable tensor $\tilde{\mathbf{L}}$ is identical to the scale similarity term proposed by Bardina *et al*[2] and we will comply with the terminology of a Mixed Model (LES-MM) when using this approach.

For the turbulent boundary layer near walls, we apply wall modeling such that the velocity in the first cell, and the skin-friction on the wall, matches the standard law-of-the-wall (without pressure gradient effects),

$$v^+ = \begin{cases} y^+ & \text{if } y^+ \leq 11.225, \\ \frac{1}{\kappa}\ln(y^+) + B & \text{if } y^+ > 11.225. \end{cases} \tag{5}$$

Here, $v^+ = v/u_\tau$ and $y^+ = yu_\tau/\nu$, with u_τ the friction velocity, are the commonly used normalized wall-parallel velocity and wall-normal distance respectively, $\kappa = 0.42$, and $B = 5.1$. The matching is implemented by adding a subgrid wall-viscosity ν_{BC} to the molecular viscosity ν in the first cell of the wall so that the sub-grid viscosity becomes,

$$\nu_{eff} = \nu + \nu_{sgs} = \frac{\tau_w}{(\partial v/\partial y)|_P} = \frac{u_\tau y_P}{v_P^+}, \tag{6}$$

where the subscript P denotes that the quantity is to be computationally evaluated at the first grid point away from the wall and τ_w is the wall shear stress.

2.2 Finite volume method

LES needs high accuracy in both space and time in order to represent the transient nature of the flow and to avoid masking the modeled influence of the sub-grid scales by truncation errors. Typically, the filter width Δ is induced by a measure of the local grid size $|\mathbf{d}|$, i.e. $\Delta \propto |\mathbf{d}|$, which makes the sub-grid tensor an $\mathcal{O}(|\mathbf{d}|^2)$-term and thus setting the lower limit of order for the discretization schemes as well. A natural choice is to use the cube root of the cell volume, $|\mathbf{d}| = V^{1/3}$, in the explicit subgrid models of LES.

The computations are made with an unstructured finite volume method implemented in the open source software package OpenFOAM, using discretization schemes which are formally second order accurate in both time and space. The equations are treated using a segregated approach where each equation is treated seperately and solved sequentially[7]. The velocity-pressure coupling is handled using a PISO-type procedure. The approach leads to a CFL-number restriction, and a CFL-number below 0.5 is preferred to achieve adequate numerical stability and accuracy. An efficient MPI implementation has been used for running on parallel computers.

The discretization scheme used is a central differencing scheme with different TVD limiters applied to the convective term to ensure stability and introduce the necessary dissipation, in case of implicit modeling. The implementation of limiters in OpenFOAM allows for parameter γ switching between best accuracy ($\gamma = 0$) and best stability ($\gamma = 1$). The base line scheme used in these simulations is thus a central differencing with a van Leer limiter applied for the convective terms and pure central differencing for the remaining terms.

For simulations with a moving computational grid, the solver is modified to implement the mesh motion while respecting the so-called discrete space conservation law[4], which is particularly important for incompressible flow simulations.

2.3 A moving mesh CFD-method

We describe a method, developed at FOI, which can be used to address problems with large boundary motion, such as a rotating component. The method is based on deformation and regeneration (D&R) of the computational grid. Here we give an overview of the D&R-method on an algorithmic level. This description is general, for instance it is not restricted to considering rotational motion. The use of the method in practice is then illustrated in the section describing the submarine simulation. The D&R-method is described in more detail in the papers by Liefvendahl and Troëng[21,22]

We talk generally about a *moving* meshes and differentiate between mesh *deformation* and the change of mesh *topology*. By topology, we mean here the connectivity of the mesh, i.e. the list of neighboring cells of each cell. A deforming mesh does not change topology but the mesh nodes are moving, thereby deforming the cells.

The D&R-method can be described in a very general setting[21] On this level of generality, the method is to "dynamically" (during the time-stepping) decide, based on an
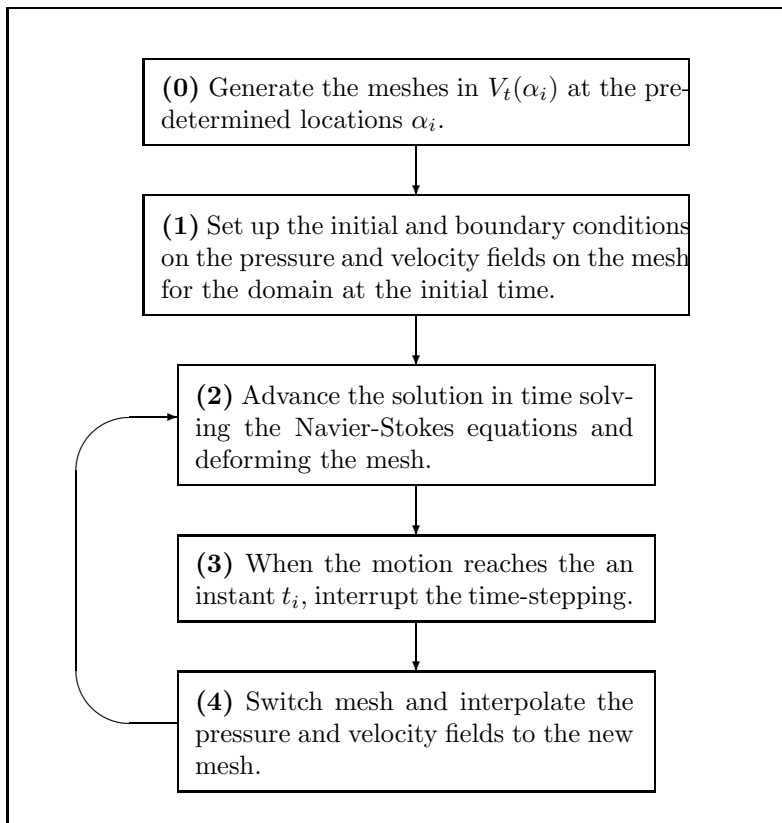
Figure 1: Flow chart for the D&R-method applied to the restricted class of problems with prescribed one-parameter motion of the boundary.

appropriate mesh quality measure, when to regenerate the mesh, and also, in which part of the complete simulation domain this is to be done. In this paper we restrict ourselves to prescribed boundary motion described by one parameter and taking place in a part of the computational domain which can be identified before the simulation is started. The reason for this restriction is that it makes it possible to make a parallel implementation which takes advantage of the specific properties, of this restricted situation, to address issues of the parallel performance and load balancing. Two applications in the field of naval hydrodynamics which fit this framework are rudder motion and propeller rotation. Other application areas include e.g. piston motion in internal combustion engine simulations.

In the above setting, we assume that the moving domain $V(\alpha) \subset \mathbf{R}^3$ can be decomposed into a disjoint union of three regions,

$$V(\alpha) = V_f \cup V_t(\alpha) \cup V_{rb}(\alpha).$$

Here $\alpha \in \mathbf{R}$ is the parameter describing the motion and V_f denotes a fixed region where the same mesh can be used throughout the simulation. The region V_{rb} moves as a rigid body and here the same mesh, submitted to the rigid-body rotation, is also used during

the simulation. The preceeding two regions are matched together by a transition region V_t. It is in the transition region that the deformation and regeneration of the mesh takes place. The computational grid is boundary fitted, meaning that it covers $V(\alpha)$ and does not extend outside of $V(\alpha)$. This construction is illustrated for the submarine simulation, where the hull is contained in V_f, the rotating propeller in V_{rb} and the transition region V_t is located between two concentric cylinders which are the boundary to the other two sub-domains.

Since the boundary motion is described by one parameter it is possible to generate the necessary meshes in V_t before the flow simulation is started. Suppose that the motion will take place in the interval $\alpha \subset [A_L, A_R]$, then this interval can be divided into subintervals where (topologically) different meshes are used. For this we introduce α_i according to,

$$A_L = \alpha_0 < \alpha_1 < ... < \alpha_i < ... < \alpha_n = A_R.$$

The i:th mesh is then used in the interval $\alpha \in [\alpha_{i-1}, \alpha_i]$ and for motion in this interval, the mesh is deformed. When the motion reaches one of the end points of this interval, we switch mesh to the one "covering" the corresponding interval. The numbers α_i and the corresponding $V_t(\alpha)$-meshes should be constructed by taking the following trade-off into account. Large α-intervals lead to poor quality mesh near the ends of the interval but at the same time leads to few mesh switches. Typically the meshes in V_t are constructed using automatic tet-meshing, at the center of the corresponding α-interval. Since the motion is prescribed, the parameter is a (given) function of time $\alpha = \alpha(t)$. Thus the mesh switching locations α_i corresponds to mesh switching instants t_i such that $\alpha_i = \alpha(t_i)$.

In figure 1, we show a flow chart illustrating the complete D&R-method. Steps (0) and (1) are carried out during the pre-processing stage. Step (2) corresponds to an LES with a deforming mesh. The topology change of the grid is described in steps (3) and (4) where we switch to the new grid (in V_t) by interpolating the flow field to it. After the interpolation, we have a grid with good quality and we can continue the solution on a deforming mesh, Step (3). The application of the D&R-method is demonstrated in the submarine section below, see figure 7.

3 A VALIDATION STUDY FOR FLOW PAST A SURFACE MOUNTED 3D HILL

The computational methodology described above, involving the OpenFOAM platform[7], has been verified and validated for a wide range of problems of incompressible flow at high Reynolds number. The performed validation studies include relatively simple turbulent flows such as channel flow and isotropic homogenenous turbulence developed from Taylor Green vortices. The case presented in this section represents an intermediate level of complexity, and consists of a validation problem designed for the investigation of the separation of a turbulent boundary layer at a smooth surface. The following sections of the paper illustrate validation with experimental data from model tests, of ship and propeller hydrodynamics.

The flow past a surface mounted 3D hill in a rectilinear channel has been experimentally studied by Simpson *et al*[9,12]. The experiments feature a h=0.078 m high, 3D axisymmetric hill, mounted on the centre floor of a 3.2h high wind tunnel. The inlet speed is v_0=27.5 m/s resulting in a Reyolds number of Re = 130,000. The experimental test section is 97.7h long and 38.8h wide. This case is challenging due to the complicated flow physics developing around the hill, and has thus been used as a challenging benchmark case for RANS and LES. Among the first to computationally address this flow was Patel *et al*[11], who successfully attempted to perform LES in a short domain of length 12h. Haase *et al*[14], report results from primarily RANS with a wide variety of two-equation RANS models and a few differential stress RANS models, and these results clearly indicate that all investigated RANS models fail to predict the dominating flow structures in the wake. Persson *et al*[17], used a short and a long computational domain, with lengths 12h and 35h, each discretized using a coarse and a fine grid, with 1.1, 2.2, 4.2 and 8.4 Mcells ($=10^6$ cells), respectively, to study the predictive capabilities of RANS, DES and LES. The results obtained support the findings of Haase *et al*[14], in that RANS cannot predict this flow with acceptable accuracy. Depending on the boundary conditions employed DES can be made to mimic both the RANS results and the more accurate LES predictions that agree well with the data of Simpson *et al*[9,12], with the exception of the rms-velocity fluctuations being underpredicted. Visbal *et al*[29], report results with LES as well as with RANS, in a domain of length 16h, with the RANS results being less accurate when compared with the experimental data, and the LES results in good agreement with those of Persson *et al*[17]. More recently, Garcia-Villalba *et al*[31], have performed high and very high resolution LES, using the dynamic Smagorinsky model, with 34 and 134 Mcells, respectively, in a domain of length 20.0h. In all cases, the computational domains contain a part of the wind tunnel, where no-slip boundary conditions are used on the top and bottom walls and slip conditions are used on the two sides. Only Garcia-Villalba *et al*[31], have compared their LES with the most recent experimental data of Ma & Simpson[15], being in better agreement with the above LES.
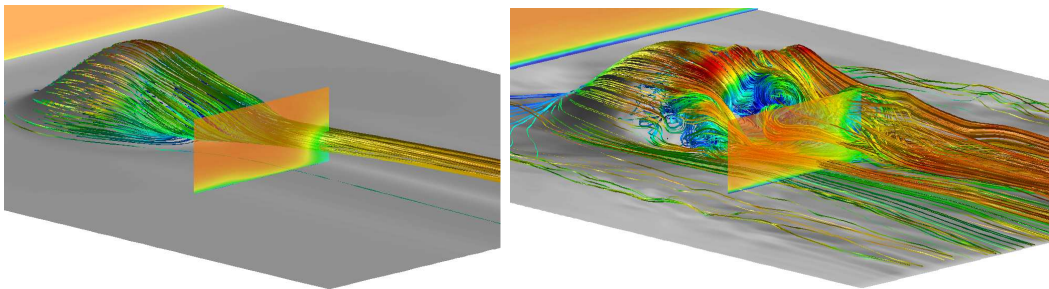

Figure 2: Flow past a 3D axisymmetric hill at Re=130,000 in terms of streamlines colored by the axial velocity, contours of the axial velocity on the measurement plane and contours (in gray) of the friction velocity on the bump surface. (a) RANS and (b), instantaneous LES using LES-MM (Mixed Model).

In figure 2, we present instantaneous flow visualizations using streamlines colored by

the axial velocity, v_x, axial velocity contours in the experimental measurement plane and friction velocity contours (in gray) on the wall from RANS and LES. Based on the LES predictions we find that owing to the gradual and smooth variation in the bump profile near the lower tunnel wall, the incident flow passes without any significant upstream separation or the appearance of a horseshoe vortical structures. As the boundary layer flow approach the leading face of the hill, the pressure increases, but not enough to cause separation, after which it gradually decrease near the top of the hill, when the flow is accelerated. As seen in figure 2, there is a pronounced acceleration of the flow over the crest of the hill followed by an unsteady shallow separation on the leeward side of the hill. The separation of the flow passing over the hill occurs when the streamwise flow from above meets the backflow created by streamlines coming from the sides of the hill, creating a complex flow pattern characterized by a saddle point of separation on the symmetry line and by two stable foci on either side of the symmetry plane. The unsteadiness of the flow includes a characteristic low-frequency meandering[31].
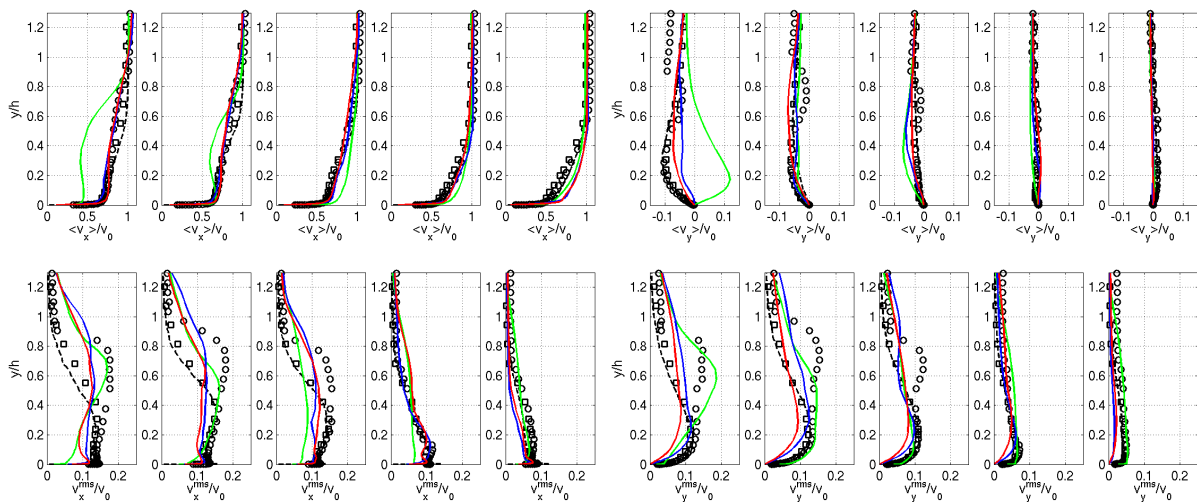

Figure 3: Flow past a 3D axisymmetric hill at Re=130,000. Comparison of the time-averaged velocity and rms velocity fluctuations at x/h=3.69. Legend: (o) experimental data[12], ($\times$) experimental data[15], (*green*) RANS of Persson *et al*[17], (− −) very fine grid LES of Garcia-Villalba & Rodi[31], (*blue*) coarse grid LES of Persson *et al*[17] using LES-MM, and (*red*) coarse grid LES-LDKM.

In figure 3, we have collected time-averaged velocity and rms-velocity fluctuation profiles from the RANS of Persson *et al*[17], the coarse grid LES of Persson *et al*[17], (using LES-MM), the very fine grid LES of Garcia-Villalba & Rodi[31], (using LES-DSMG) and a recently performed LES (using LES-LDKM[6]). These predictions are compared with the experimental LDV data of Byun & Simpson[12], and the hot-wire data of Ma & Simpson[15]. The Ma & Simpson[15], data is considered the most accurate since the LDV data is associated with a seeding problem in the wake that becomes apparent in the second order statistical moments. The difference between these two experimental data sets is small but

9

not negligible for the time-averaged velocity components, $\langle v_i \rangle$, but is substantial for the rms-velocity fluctuation components, v_i^{rms}. These difference are not easy to explain but according to Garcia-Vilalba *et al*[31], the differences are attributed to the two measurement techniques, and it is argued that the data of Ma & Simpson[15], is the more accurate of the two. Concerning the RANS predictions we find that these predictions do not capture the basic features of the flow with poor predictions of both $\langle v_i \rangle$ and v_i^{rms}. These RANS results are good representatives of the approach as may be observed by comparing also with other RANS results[14]. The very fine grid LES of Garcia-Villalba & Rodi[31], show excellent agreement with the experimental data of Ma & Simpson[15], but less good agreement with the data of Byun & Simpson[12], suggesting that the Ma & Simpson data, is the more reliable. The coarse grid LES of Persson *et al*[17], and the recent LES-LDKM, show good agreement for the time-averaged velocity, $\langle v_i \rangle$, with both experimental data sets, but with some underprediction of $\langle v_y \rangle$ close to the centerline. For v_i^{rms} the agreement is less accurate than for the time-averaged velocity, but still reasonable, with the LES-LDKM showing the best agreement with the experimental data. These results indicate that even on a coarse grid the LES-MM and the LES-LDKM model can capture the complex flowfield developing around the surface mounted 3D hill.

4 STAND-ALONE PROPELLER SIMULATION

We present results for a generic submarine propeller in open water conditions. In the experimental procedure, this correspond to tests of the stand-alone propeller in a cavititation tunnel. For the computations, we consider the propeller rotating at constant speed in a uniform inflow.

For submarine propellers there are extreme requirements on the reduction of the generated noise and vibrations. This has oriented designers towards complex configurations of the blade system, in order to minimize the blade load gradients along the azimuth as well as to avoid coupling with the perturbations caused by the incoming flow. More specifically, a typical approach is the adoption high blade number (7 here) and highly skewed blades with a tip unloading design. The propeller is shown in figure 4, and it is the same model we use in the submarine simulations of the next section. The propeller is denoted E1619, and was designed at the Italian Ship Model Basin (INSEAN). The experiments were carried out in the INSEAN Large Circulating Water Channel and concerned Laser Doppler Velocimetry (LDV) measurements of the velocity distribution in three cross-planes of the wake, at three values of the advance ratio[30].

This configuration has been simulated for a range of advance number, on several grids of different refinement level, ranging from $2 \cdot 10^6$ to $13 \cdot 10^6$ cells[30,32]. To account for the propeller motion, we simulate it in an inertial reference frame and rotate the grid, as a rigid body with the propeller. The methodology, has been throughly validated for other propeller flows as well[26]. For this type of applications, the industrial standard is to employ potential flow or RANS methods. The motivation for the use of LES is situations where unsteady phenomena (in the rotating frame of reference) are important. This includes
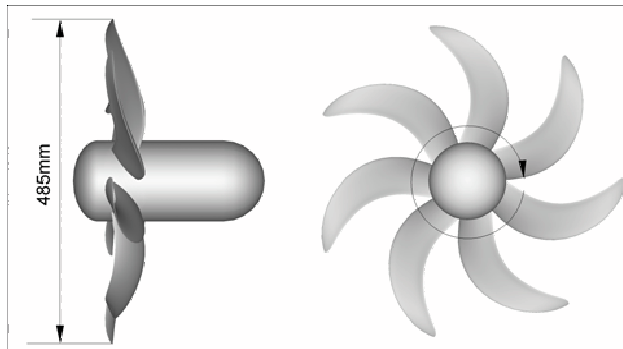
Figure 4: Geometry of the INSEAN E1619 propeller.

the following. (1) Simulation of the appended propeller operating in the unsteady wake flow, see the submarine section. (2) Investigation of propeller wake instability, see figure 6 below. (3) Caviation simulations, where LES captures, at least partially, the dynamics of the cavitation bubble[25].

Quantity	Notation	Expression	Unit	Value
Propeller diameter	D_P	-	m	0.485
Inflow velocity	V_∞	-	m/s	1.68
Kinematic viscosity	ν	-	m^2/s	10^{-6}
Propeller rotation freq.	n	-	1/s	4.68
Advance number	J	$V_\infty/(nD_P)$	-	0.74

Table 1: Parameters and notation.

The thrust and torque, which are integrated quantities, are well predicted also on the coarser meshes and all simulations give a discrepancy of less than 5% for thrust and torque, as compared to the measured values, in the range of tested advance numbers. Below we present flow results for the advance number given in table 1, which correspond to slightly higher loading than at the design point for the propeller. We focus on results from the computations on the fine grid with $13 \cdot 10^6$ cells.

The near wake of the propeller consists of several sharp flow structures and their interaction. The flow is dominated by the tip-vortices, the blade wakes and the complex flow originating at the blade roots and interacting with the hub vortex. As compared to a standar propeller, the tip vortices are significantly weaker for this configuration. During the spiralling motion downstream, a bending of the blade wakes occur which leads to interaction between successive blade wakes. This occurs at a certain position downstream which depend on the loading condition and the propeller design. In figure 5, we show the mean axial velocity in a cross-plane close to the propeller. We see that the solution on the coarse mesh does cannot well resolve the sharp blade wakes, even this close to the propeller. For the fine mesh, on the other hand, the shape of the blade wakes and tip-
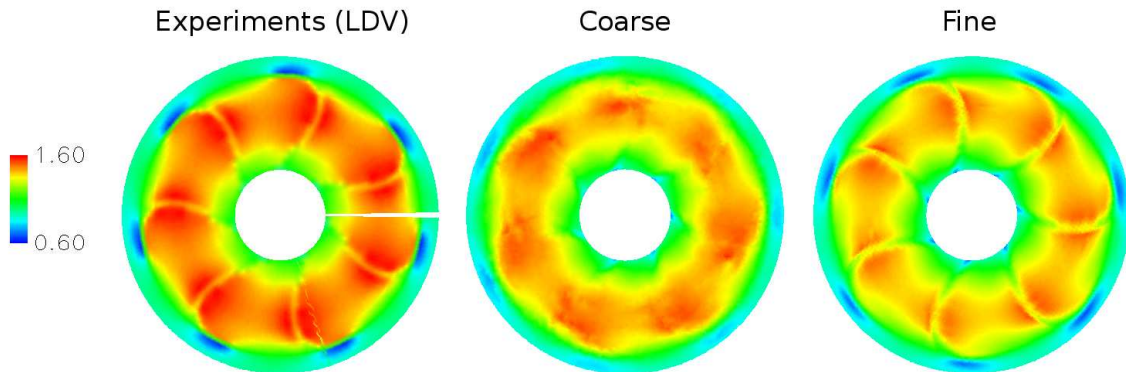
11

Figure 5: Normalized axial velocity in the plane $x/R_p = 0.17$. LDV measurements to the left, simulations on a coarse mesh with $2.6 \cdot 10^6$ cells in the center and simulations on the fine mesh, with $13 \cdot 10^6$ cells, to the right.

vortices are well predicted. An illustration of the capability of LES to provide essentially more information about the flow field than RANS or potential methods, is the application to investigate wake instability[32]. Here the dynamics of the large scale flow structures is the significant phenomena, and a time-resolved solution is necessary in order to investigate it. In the simulations, we have placed a large number of probes in fixed locations relative to the propeller, i.e. rotating with it. In figure 6, we illustrate the location of one set of probes. In the probes we collect the complete time history, of the velocity and pressure fields, during the time advancement with a time step $\Delta t = 20 \, \mu s$.

In figure 6, we present data, both in time and frequency domain (obtained by Fourier transform) from two probes in the near wake. The probes are located close to each other but exhibit very different behaviour, which illustrate the rapid change in character of the flow in the propeller wake. Probe (133) show fluctuations in the axial velocity of about 5% whereas the fluctuations for probe (121) are less than 1%. Very interesting to note, is the tonal contribution in the spectrum of probe (133) at 230 Hz (and the smaller peak at twice this frequency). A crude estimate of the vortex shedding frequency from the trailing edge of the blade can be based on the blade thickness, the flow velocity relative to the blade and the Strouhal number for vortex shedding from a cylinder ($S \approx 0.21$). This estimate gives a shedding frequency of 147 Hz, which indicates that the peak in figure 6 may correspond to vortex shedding at the blade trailing edge[32].

5 SUBMARINE HYDRODYNAMICS

The simulation presented in this section represents a major step forward, as compared with established methods, concerning the level of detail in the modeling of the flow in the stern region and around the propeller. The configuration is a generic submarine hull[3], denoted AFF8, which has been designed at the David Taylor Research Center (USA), and
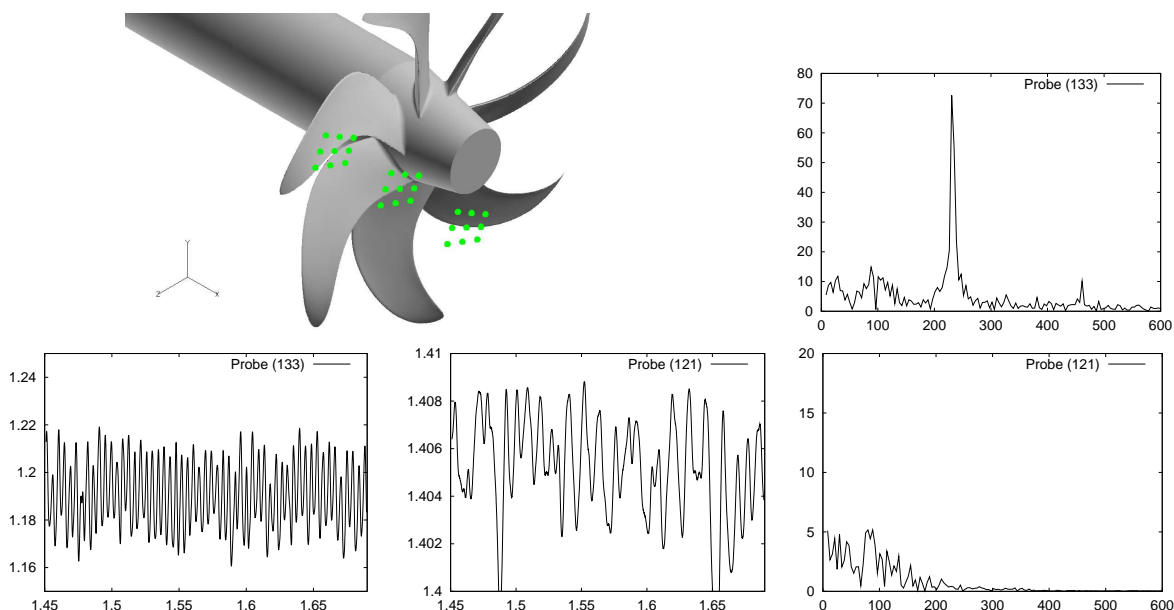
Figure 6: Probe data in the propeller wake. 27 probe locations, in three cross-planes, are indicated with green dots, relative to the propeller. Time signal for the normalized axial velocity, and the corresponding spectrum, are shown for probe (121) and (133), which are located in the cross-plane closest to the propeller. Probe (133) is situated in a blade wake at radius $0.9R_p$ and probe (121) is situated just outside a blade wake, at radius $0.8R_p$. The two time plots, for $t \in (1.45, 1.69)\, s$, are placed below the propeller picture and the two spectra, in the frequency interval $(0, 600)\, Hz$ are shown to the right.

the E1619 propeller described in the section above. Since a complete propeller model in included, and the computation is carried out with high mesh resolution ($\mathcal{O}(10^7)$ cells), it is possible to investigate the temporally and spatially resolved flow field around the hull and the propeller.

	# Mcells	# Proc.	Mcells/Proc.
Total	$8.15 \cdot 10^6$	20	$0.41 \cdot 10^6$
V_f	$6.26 \cdot 10^6$	14	$0.47 \cdot 10^6$
V_{rb}	$1.53 \cdot 10^6$	5	$0.31 \cdot 10^6$
V_t	$0.36 \cdot 10^6$	1	$0.36 \cdot 10^6$

Table 2: Size of the computational mesh in terms of the number of cells in the three sub-regions. The distribution of cells on processors for parallel computation is indicated in columns three and four. The values in the second and fourth column are given in Mcells ($=10^6$ cells).

The mesh generation procedure is quite complicated for this problem both because of the dynamic grid framework of the D&R-method, and because of the difference in length scale of the geometrical details (e.g. hull vs propeller blade). General recommendations are to use hexahedral (hex-)cells in the mesh for a hull simulations and, due to the geometric complexity, an unstructured mesh for the propeller. This unstructured mesh
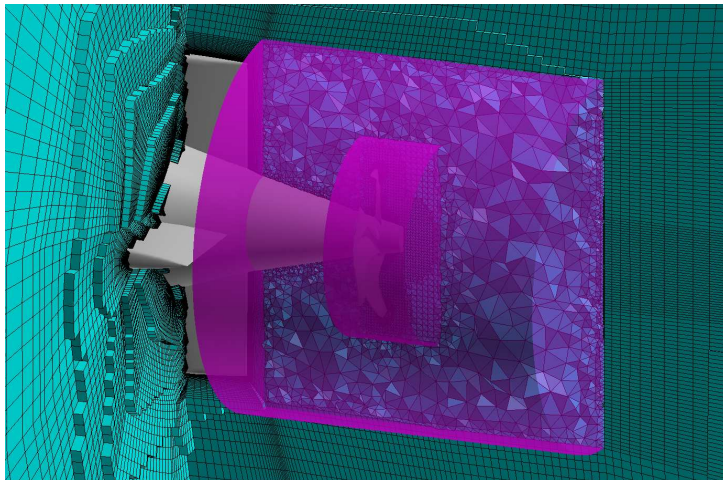
13

Figure 7: Illustration of the D&R-regions for the submarine simulation. The fixed region V_f outside the cylinders, the rigid body region V_{rb} around the propeller in the inner cylinder, and the transition region V_t in between the concentric cylinders. The volume mesh is also illustrated on the center plane and a cross-plane cutting the stern rudders.

consists of tetrahedral (tet-)cells in the main part of the volume and a number of layers of prismatic (prism-)cells to resolve the boundary layer on the blades, hub and shaft. The boundary layer on the hull is captured with hex-cells with high aspect ratio (flat cells). In the complete D&R-simulation we thus have cells of three types: hex, tet and prism. The mesh is illustrated in figure 7, together with the cylinders which bound the domains of the different sub-regions used in the D&R-method. During one rotation, we use 18 topologically different meshes which have been pre-generated. Each mesh thus covers, by deformation an interval of 20° rotation of the propeller. The total mesh size, and the size of the mesh in the sub-regions, are given in table 2.

To obtain a good load balance when running on parallel computers, is a crucial difficulty for any CFD-method with a topologically changing grid. This is discussed in detail, in connection with the D&R-method[28], for a similar submarine-propeller configuration as the one discussed here, but with a smaller mesh ($\mathcal{O}(10^6)$ cells). It was shown that a parallel speed-up can be obtained, which is comparable to fixed grid simulations, for the D&R-method for submarine-propeller configurations. The different sub-regions are distributed on separate sets of processor, and the resulting load balancing is summarized in table 2.

The submarine has been simulated, with the LES-OEEVM subgrid model, on a straight course, with a constant speed (corresponding to Re=$12.8 \cdot 10^6$, and with a constant load on the propeller (advance number $J = 1.1$). The data sampling and post-processing possibilities are virtually unlimited for this type of simulation. As for the standard case, it is possible to investigate the mean flow and rms-fluctuations around the hull and propeller, as well as the thrust and torque of the propeller operating behind the hull. An averaging procedure which is phase-sampled with the propeller position, is also of high interest in
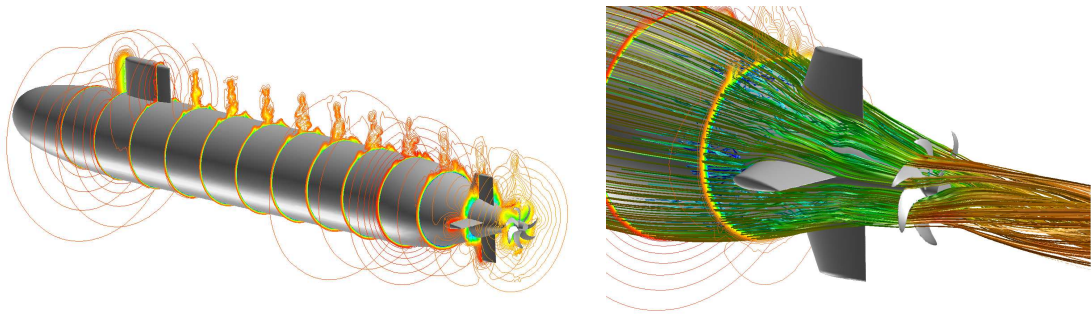
Figure 8: Overview of the computed flow around the AFF8 submarine hull with the INSEAN E1619 propeller. In the left picture, we have the axial velocity in cross-planes in the zoom on the stern, to the right, we also include streamlines, colored by magnitude of velocity.

the stern region. Further possibilities, using the computed time-resolved flow, include the investigation of the motion of the large scale structures around the hull, the fluctuating pressure forces on parts of the propeller and hull and probe data for the different turbulent regions. Below we only give two examples illustrating the computed flow.

The flow around the hull and the propeller is shown in figure 8. These visualizations present the overall structure, with the turbulent sail wake, the horseshoe vortex from the sail, the more complex flow over the stern and around the stern rudders and the interaction of the propeller action with the incoming flow.
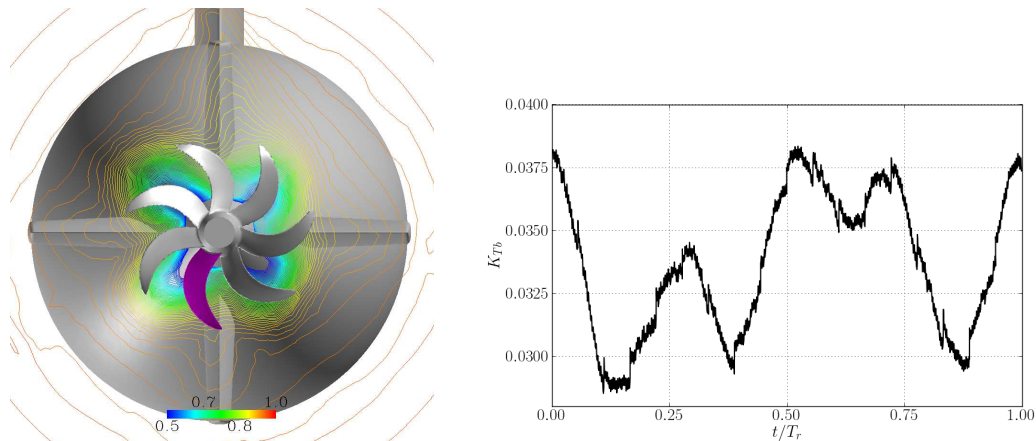

Figure 9: Contribution to the thrust from one propeller blade, K_{Tb}. The blade is in the left figure relative to the inflow which is indicated by the axial velocity on a cross-plane just upstream of the propeller. To the right, K_{Tb} is plotted versus time, during one propeller rotation, T_r.

From the perspective of noise generation, it is important to investigate the fluctuating loads on the propeller, which are related both to flow generated noise and induced vibrations. In figure 9, we show the time evolution of the contribution to the thrust from one single propeller blade. In the left picture, the dedicated blade is shown relative to the

inflow to the propeller. In that position, it enters a low velocity region, which is translated to the high blade load we see in the line plot at $t/T_r = 0$, which is the corresponding time. During the rotation, we identify four peaks (of different shape) in the blade load, which corresponds to the four regions with low velocity, seen in the left picture.

6   SURFACE SHIP HYDRODYNAMICS

We present results for the flow past the DTMB 5415 surface combatant hull[8,13,24]. Both experimental data[8], and computational results from previous RANS, DES and LES[13,23,24], are available for comparison, making this case an ideal platform for evaluating different models. An additional reason for selecting this case is that it have been used as a validation platform for experimental studies by Iowa Institute of Hydraulic Research, the Italian Ship Model Basin and the David Taylor Model Basin.

Figure 10(a), shows a perspective view from the stern oft the DTMB5415 hull in terms of an iso surface of the volume fraction of water colored by the wave height, streamlines colored by the air velocity released at the bow and an iso-surface of the second invariant of the velocity gradient tensor illustrating the flow developing around the submerged part of the hull. The typical size of these computations range between 10 and 20 Mcells for a model scale Reynolds-number of Re$\approx$12·10^6 and a Froude number of Fr$\approx$0.28, that can be compared with towing tank measurement data. For the computations performed here block structured grids are used with refinement patches in the hull boundary layer, around the water surface and in the wake. In figure 10(b), we compare predicted and measured[8] wave elevations at Re$\approx$12·10^6 and Fr$\approx$0.28, revealing that the experimentally obtained wave profiles are slightly higher and sharper than what can be obtained using the adopted volume-of-fluid (VoF-)approach[24]. Capturing the developing wave pattern is a computationally very challenging task due to the large density ratio between air and water and since the interface is generally thin, but may include breaking bow waves (at high Fr numbers) that develop foam as well as entrained air beneath the hull.
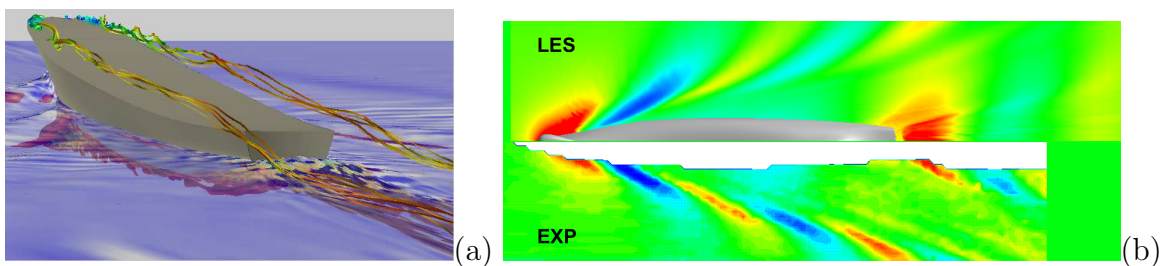

Figure 10: Flow past the DTMB5415 surface combatant hull. (a) Perspective view from the stern showing the vortex structures developing over the bow, the Kelvin wave pattern and some flow structures developing around the submerged part of the hull. (b) Comparison of predicted (LES) and measured (EXP) surface wave deflection pattern at Re=12·10^6 and Fr=0.28.

In figure 11(a) and 11(c), the flow past the DTMB 5415 hull from LES-LDKM and DES,
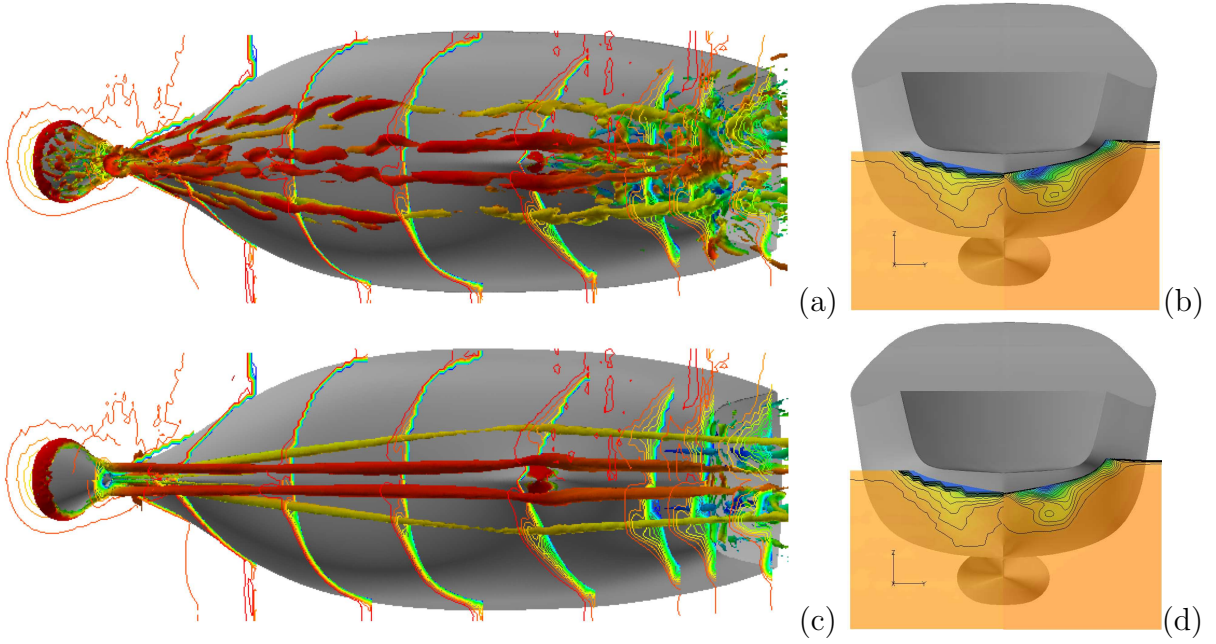
Figure 11: Flow past the DTMB5415 surface combatant hull. (a) and (c) instantaneous flow visualizations from LES-LDKM and DES models, respectively, in terms of iso-surfaces of the second invariant of the velocity gradient, colored by the axial velocity, and contours of the axial velocity at eight sections across the hull. (b) and (d) contours of the axial velocity at x/L=0.9346 from experiments (left) and predictions using LES-LDKM and DES (right), respectively.

respectively, is presented in terms of iso-surfaces of the second invariant of the velocity gradient, colored by the axial velocity, and contours of the axial velocity at eight sections across the hull. The view is from underneath the ship with the large sonar dome to the left and the transom stern to the right. These instantaneous figures show dramatically different coherent structures resulting from the two simulations, with the DES results showing only two pairs of almost stationary vortex structures developing from the trailing edge of the sonar dome and the junction between the hull and sonar dome respectively. The LES-LDKM results on the contrary show a much more vigorous flow with more unsteady structures developing along the hull. In both cases, additional structures develop beneath the transom stern where viscous flow effects starts to become more important. Two propellers are located under the transom stern, on each side of the skeg, in a region of unsteady flow dominated by several pairs on unsteady vortical structures. The ability to correctly predict the unsteady dynamics of these vortex systems is imperative for the design of improved ships with better performance and comfort. In figures 11(b) and 11(d), we compare predictions from the LES-LDKM and DES models with experimental data[8], at x/L=0.9346. The left hand half of these figures is the experimentally obtained mean axial velocity whereas the right hand half are the LES-LDKM and DES predictions, respectively. Although the instantaneous flow appears different, the time averaged flow from both these models agree well with the experimental data. Similar agreement is found

17

at all eight cross sections along the hull at which experimental data is available. Besides providing new information about the flow past the DTMB 5415 hull, this comparison highlights the complexity when comparing predictions and experimental data.

7 CONCLUDING REMARKS

We have reviewed a computational methodology for naval hydrodynamics and its application to a series of challenging problems in the field. The two most advanced contributions concern the application of LES to these classes of problems, and the moving mesh method, and its demostrated capability to perform coupled propeller-hull simulations with high temporal and spatial resolution. The results for the validation case, with separated flow at a smooth surface, illustrates certain short-comings of RANS methods, as compared to LES, in terms of predictive accuracy of this important flow phenomena. We evaluated the capability to capture the different, very sharp, flow structures in the near wake of a submarine propeller, by comparison with LDV flow measurements. A fully appended submarine simulation has been carried out, which demonstrates the state of the art, in particular concerning the complex flow at the stern and around the propeller. An increased understanding of the processes involved here are highly important from the point of view of propeller noise minimization. Finally, we illustrated the capabilites for simulation of a surface ship, with a validation study concerning the wave pattern and the flow under the ship. The methods described in the present chapter are beeing developed at a rapid pace and we have tried to provide suggestions and evaluations concerning the advantages and drawbacks of time-resolved, LES-based methods, as compared with experimental methods and less computationally expensive CFD, for the selected problems in naval hydrodynamics.

REFERENCES

[1] U. Schumann, Subgrid scale model for finite difference simulation of turbulent flows in plane channels and annuli, *J. Comp. Phys.*, **18**, 376-404, (1975).

[2] J. Bardina, J. H. Ferziger and W. C. Reynolds, Improved subgrid scale models for Large Eddy Simulations, *AIAA Paper*, 80-1357, (1980).

[3] N. C. Groves, T. T. Huang and M. S. Chang, Geometric characteristics of DARPA SUB-OFF models, Technical Report, DTRC/SHD-1298-01, David Taylor Research Center, USA, (1989).

[4] I. Demirdžić and M. Perić, Finite Volume Method for Prediction of Fluid Flow in arbitrarily shaped domains with moving boundaries, *Int. J. Numerical Meth. Fluids*, **10**, 771-790, (1990).

[5] D. C. Wilcox, Turbulence Modelling for CFD, *DCW Industries*, (1993).

[6] S. Menon and W. Kim, High Reynolds number flow simulations using the Localized Dynamic Subgrid-Scale Model, *AIAA Paper*, 96-0425, (1996).

[7] H. G. Weller, G. Tabor, H. Jasak and C. Fureby, A tensorial approach to CFD using object oriented techniques, *Comp. in Physics*, **12**, 620-631 (1997).

[8] A. Olivieri, F. Pistani, A. Avanzini, F. Stern and R. Penna, Towing tank experiments of resistance, sinkage and trim, boundary layer, wake and free surface flow around a naval combatant INSEAN 2340 model", Iowa Institute of Hydraulic Research, Technical Report 421, (2001).

[9] R. L. Simpson, C. H. Long and G. Byun, Study of vertical separation from an axisymmetric hill, *Int. J. Heat and Fluid Flow*, **23**, 582-591 (2002).

[10] G. Constantinescu, M. Chapelet and K. Squires, Turbulence modeling applied to flow over a sphere, *AIAA Journal*, **41**, 1733-1742, (2003).

[11] N. Patel, C. Stone and S. Menon, Large Eddy Simulation of Turbulent Flow over and Axisymmetric Hill", *AIAA Paper*, 03-0967, (2003).

[12] G. Byun and R. L. Simpson, Structure of three-dimensional separated flow on an axisymmetric bump, *AIAA Paper*, 2005-0113, (2005).

[13] G. B. Deng, E. Guilmineau, P. Queutey and M. Visonneau, Ship flow simulations with ISIS CFD code", In proceedings of the *CFD workshop*, T. Hino Ed, Tokyo, Japan, (2005).

[14] W. Haase, B. Aupoix, U. Bunge and D. Schwamborn, FLOWMANIA Flow-Physics Modeling - An integrated approah. Notes on Numerical Fluid Mechanics and Multidisciplinary Design, *Springer Verlag, Berlin*, (2005).

[15] R. Ma and R. L. Simpson, Characterization of turbulent flow downstream of a three-dimensional axisymmetric bump, In proceedings of the *4th Int. Symp. on Turbulent and Shear Flow Phenomena*, Williamsburg, USA, (2005).

[16] N. J. Georgiadis and J. R. DeBonis, Navier Stokes Analysis Methods for Turbulent Jet Flows with Application to Aircraft Exhaust Nozzles, *Prog. Aerospace Sci.*, **42**, pp. 377, (2006).

[17] T. M. Persson, M. Liefvendahl, R. Bensow and C. Fureby, Numerical investigation of the flow over an axisymmetric hill using LES, DES and RANS, *J. Turbulence*, **7**, pp. 1, (2006).

[18] P. Sagaut, Large Eddy Simulation for Incompressible Flows, 3rd Ed., *Springer Verlag*, (2006).

[19] R. E. Bensow and C. Fureby, On the justification and extionsion of Mixed Models in LES, *J. Turbulence*, **8**, (2007).

19

[20] F. F. Grinstein, L. G. Margolin and W. J. Rider Eds., Implicit Large Eddy Simulation: Computing Turbulent Fluid Dynamics, Cambridge University Press, (2007).

[21] M. Liefvendahl and C. Troëng, Deformation and regeneration of the computational grid for CFD with moving boundaries, In proceedings of the *45th AIAA Aerospace Sciences Meeting and Exhibit*, AIAA-2007-1458, Reno, USA (2007).

[22] M. Liefvendahl and C. Troëng, *Simulation of incompressible flow with large boundary motion by deforming and regenerating the computational mesh*, In proceedings of the *OpenFOAM International Conference*, Windsor, UK (2007).

[23] J. Yang, N. Sakamoto, Z. Wang, P. Carrica and F. Stern, Two-phase level-set/immersed-boundary cartesian grid method for ship hydrodynamics, In proceedings of the *9th Int. Conf. on Numerical Ship Hydrodynamics*, Ann Arbor, USA, (2007).

[24] N. Alin, C. Fureby, O. Parmhed and U. Svennberg, Large Eddy Simulation past the DTMB 5415 Hull, In proceedings of the "27th Symposium on Naval Hydrodynamics", Seoul, Korea, (2008).

[25] R. E. Bensow, T. Huuva, G. Bark and M. Liefvendahl, *Large Eddy Simulation of Cavitating Propeller Flows*, In proceedings of the *27th Symposium on Naval Hydrodynamics*, Seoul, Korea, (2008).

[26] R. E. Bensow and M. Liefvendahl, *Implicit and explicit subgrid modeling in LES applied to a marine propeller*, In proceedings of the *38th Fluid Dynamics Conference and Exhibit* AIAA-2008-4144, Seattle, USA (2008).

[27] C. Fureby, Large Eddy Simulation of Ship Hydrodynamics, In proceedings of the *27th Symposium on Naval Hydrodynamics*, Seoul, Korea (2008).

[28] M. Liefvendahl and C. Troëng, *Parallelization and Load Balancing of a Dynamic Mesh Method for Moving Boundary CFD*, In proceedings of the *Opensource CFD, Int. Conf.*, Berlin, Germany (2008).

[29] M. R. Visbal, D. P. Rizzetta and J. Matthew, Large Eddy Simulation of turbulent flow past a 3D bump, *AIAA Paper* 2007-0917 (2008).

[30] F. Di Felice, M. Felli, M. Liefvendahl and U. Svennberg, Numerical and experimental analysis of the wake behaviour of a generic submarine propeller, In proceedings of the *1st International Symposium on Marine Propulsors*, Trondheim, Norway (2009).

[31] M. Garcia-Villalba, N. Li, W. Rodi and M. A. Leschinger, Large Eddy Simulation of separated flow over a three-dimensional axisymmetric hill, *J. Fluid Mech.*, **627**, pp. 55, (2009).

[32] M. Liefvendahl, Investigation of propeller wake instability using LES, *Ship Technology Research*, (2010).